INTERNATIONAL JOURNAL FOR NUMERICAL METHODS IN ENGINEERING
Int. J. Numer. Meth. Engng (in press)
Published online in Wiley InterScience (www.interscience.wiley.com). DOI: 10.1002/nme.1552

The development of hybrid axisymmetric elements based on the Hellinger–Reissner variational principle

C. S. Jog*, †, § and R. Annabattula‡, ¶

Department of Mechanical Engineering, Indian Institute of Science, Bangalore 560012, India

SUMMARY

We present a general procedure for the development of hybrid axisymmetric elements based on the Hellinger–Reissner principle within the context of linear elasticity. Similar to planar elements, the stress interpolation is obtained by an identification of the zero-energy modes. We illustrate our procedure by designing a lower-order (four-node) and a higher-order (nine-node) element. Both elements are of correct rank, and moreover use the minimum number of stress parameters, namely seven and 17. Several examples are presented to show the excellent performance of both elements under various demanding situations such as when the material is almost incompressible, when the thickness to radius ratio is very small, etc. When the variation of the field variables is along the radial direction alone, when the mesh is uniform, and the loading is of pressure type, the developed elements are superconvergent, i.e. they yield the exact nodal displacement values. Copyright © 2005 John Wiley & Sons, Ltd.

KEY WORDS: hybrid axisymmetric elements; zero-energy modes; Hellinger–Reissner principle

1. INTRODUCTION

Although classified under 'two-dimensional' problems, the design of hybrid axisymmetric elements is much more challenging than the design of planar hybrid elements. The most challenging part in a hybrid formulation is the identification of the stress interpolation—see Reference [1] for a recent overview of assumed stress methods. There has been almost universal agreement on the stress interpolation functions for lower and higher-order planar hybrid elements, and developments have mostly focused on improving the *efficiency* of such elements. In sharp contrast, widely varying interpolation functions have been used for the design of

*Correspondence to: C. S. Jog, Department of Mechanical Engineering, Indian Institute of Science, Bangalore 560012, India.
†E-mail: jogc@mecheng.iisc.ernet.in
‡E-mail: ratna@mecheng.iisc.ernet.in
§Associate Professor.
¶Graduate Student.

Received 7 December 2004
Revised 29 April 2005
Accepted 10 August 2005

axisymmetric elements, with some researchers formulating these interpolation functions in terms of global co-ordinates (e.g. References [2–5]), while others formulating them in terms of natural co-ordinates (e.g. References [6–11]). Even among these two sub-types, there seems to be no agreement, with some using many more parameters than the minimum required for a correct rank, while some others attempting to design 'optimal' elements with such a minimum number. For example, Spilker and Pian [2] propose a 22 parameter model based on global co-ordinates, while in a subsequent work, Spilker [3] uses a nine parameter model. The problem with the existing elements that use global co-ordinates, however, is that the resulting elements are quite sensitive to mesh distortion, or are not co-ordinate frame-invariant (see Reference [6]). In addition, terms of the form $1/r$ that are used in some of these formulations result in a singularity at $r = 0$ so that stresses cannot be directly computed at the axis of a solid axisymmetric body. The choice of $1/r$ type of terms seems to be motivated by the exact solution of a cylindrical hollow cylinder subjected to an internal pressure [2]. However, in some other situations, stresses may vary as r^n, $n>0$, e.g. in a steadily spinning disc, the stresses vary as r^2. Thus, as in the case of the displacement field, it is preferable to use polynomial basis functions. As we show in Section 3, it is possible to get fairly accurate coarse-mesh solutions with the use of such polynomial basis functions even though the stress dependence on r is quite diverse. The reason is that the 'β' parameters, which are related to the displacement field, are only locally constant over an element, so that as long as the displacement field varies in the correct manner, the correct stress variation is also captured.

Our goal in this work is to present a general, but simple, methodology for the design of hybrid axisymmetric elements, based on zero-energy modes, which can be used to design lower and higher-order elements. Perhaps the lack of a general methodology is best exemplified by the fact that, to the best of our knowledge, there seems to be no existing higher-order hybrid axisymmetric element in the literature (although they may exist in commercial finite element codes). We show that elements designed using this methodology possess all the desired characteristics, namely, they yield high coarse-mesh accuracy, are co-ordinate frame-invariant and insensitive to mesh distortion, are almost immune to shear locking, yield good results for almost incompressible materials, are economical since they use the least number of stress parameters needed to ensure correct rank of the stiffness matrix, and so on.

Besides possessing the above characteristics, our numerical experiments also seem to indicate that when the variation of the field variables is along one direction alone, and the loading is of pressure type, both elements yield exact nodal displacements when uniform meshes are used. This phenomenon of 'superconvergence' is known to occur in standard displacement-based one-dimensional (and one-dimensional only) finite element formulations, when the loading is of point-load type; proofs can be found in References [12, 13]. Unfortunately, these proofs cannot be extended in a straightforward way to the problem at hand due to the mixed formulation being used; a mathematical proof of this result would obviously be of interest.

The methodology presented here can be extended to non-linear elasticity problems by enforcing both, the equilibrium equation in terms of the second Piola–Kirchhoff stress on the undeformed configuration, and the non-linear strain–displacement relation, in a weak sense. The extension to inelasticity can be carried out in a manner analogous to that outlined in Reference [14].

Section 2 describes the variational formulation, and then the design of four-node and nine-node elements based on this formulation. Section 3 presents numerical results to demonstrate the performance of these elements, and Section 4 presents the conclusions.

2. VARIATIONAL AND FINITE ELEMENT FORMULATION

Let $\mathbf{u} \equiv (u_r, u_z)$ denote the displacement field, and $\boldsymbol{\tau}_c$ and $\bar{\boldsymbol{\varepsilon}}_c$ denote the stress and the linearized strain tensor $[\nabla\mathbf{u} + (\nabla\mathbf{u})^t]/2$ for the axisymmetric problem expressed in 'engineering' form, i.e. let

$$\boldsymbol{\tau}_c = \begin{bmatrix} \tau_{rr} \\ \tau_{zz} \\ \tau_{rz} \\ \tau_{\theta\theta} \end{bmatrix}, \quad \bar{\boldsymbol{\varepsilon}}_c = \begin{bmatrix} \dfrac{\partial u_r}{\partial r} \\ \dfrac{\partial u_z}{\partial z} \\ \dfrac{\partial u_r}{\partial z} + \dfrac{\partial u_z}{\partial r} \\ \dfrac{u_r}{r} \end{bmatrix} \tag{1}$$

An overbar is put on the symbol $\boldsymbol{\varepsilon}$ since the strain $\boldsymbol{\varepsilon}_c$ in the two-field variational formulation that we describe below is not computed directly using the above strain–displacement relationship. The stress and strain tensors are related as $\boldsymbol{\varepsilon}_c = \mathbf{S}\boldsymbol{\tau}_c$, where for a linear isotropic material, with E denoting the Young modulus and v the Poisson ratio,

$$\mathbf{S} = \frac{1}{E}\begin{bmatrix} 1 & -v & 0 & -v \\ -v & 1 & 0 & -v \\ 0 & 0 & 2(1+v) & 0 \\ -v & -v & 0 & 1 \end{bmatrix}$$

Let $\bar{\mathbf{t}}$ and $\mathbf{b}$ denote the prescribed tractions acting on the surface Γ_t, and the body forces, respectively, and let $(\mathbf{v}, \boldsymbol{\sigma}_c)$ denote the variations of the displacement and stress fields. Then the two-field variational formulation obtained by enforcing the equilibrium equations, traction boundary condition and the strain–displacement relation in a weak sense is given by (these equations can also be derived from the Hellinger–Reissner functional as in Reference [6])

$$\int_\Omega \boldsymbol{\sigma}_c^t[\bar{\boldsymbol{\varepsilon}}_c(\mathbf{u}) - \mathbf{S}\boldsymbol{\tau}_c]\,\mathrm{d}\Omega = 0 \quad \forall\boldsymbol{\sigma}_c \tag{2}$$

$$\int_\Omega [\bar{\boldsymbol{\varepsilon}}_c(\mathbf{v})]^t\boldsymbol{\tau}_c\,\mathrm{d}\Omega = \int_\Omega \mathbf{v}^t\mathbf{b}\,\mathrm{d}\Omega + \int_{\Gamma_t} \mathbf{v}^t\bar{\mathbf{t}}\,\mathrm{d}\Gamma \quad \forall\mathbf{v} \tag{3}$$

where for the axisymmetric domain under consideration, $\mathrm{d}\Omega$ can be taken to be $r\,\mathrm{d}r\,\mathrm{d}z$.

Let the displacement and stress fields, and their variations, be interpolated as

$$\mathbf{u} = \mathbf{N}\hat{\mathbf{u}}, \quad \boldsymbol{\tau}_c = \mathbf{P}\hat{\boldsymbol{\beta}}$$

$$\mathbf{v} = \mathbf{N}\hat{\mathbf{v}}, \quad \boldsymbol{\sigma}_c = \mathbf{P}\hat{\boldsymbol{\gamma}}$$

Substituting the above interpolations into Equations (2) and (3), and invoking the arbitrariness of $\hat{\mathbf{v}}$ and $\hat{\boldsymbol{\gamma}}$, we get the matrix equations

$$\begin{bmatrix} -\mathbf{H} & \mathbf{G} \\ \mathbf{G}^t & \mathbf{0} \end{bmatrix} \begin{bmatrix} \hat{\boldsymbol{\beta}} \\ \hat{\mathbf{u}} \end{bmatrix} = \begin{bmatrix} \hat{\mathbf{g}} \\ \hat{\mathbf{f}} \end{bmatrix} \tag{4}$$

where, with $\mathbf{B}$ denoting the 'strain–displacement matrix' (i.e. $\bar{\boldsymbol{\varepsilon}}_c = \mathbf{B}\hat{\mathbf{u}}$),

$$\mathbf{H} = \int_\Omega \mathbf{P}^t \mathbf{S} \mathbf{P} \, \mathrm{d}\Omega$$

$$\mathbf{G} = \int_\Omega \mathbf{P}^t \mathbf{B} \, \mathrm{d}\Omega$$

$$\hat{\mathbf{g}} = \mathbf{0}$$

$$\hat{\mathbf{f}} = \int_\Omega \mathbf{N}_u^t \mathbf{b} \, \mathrm{d}\Omega + \int_{\Gamma_t} \mathbf{N}_u^t \bar{\mathbf{t}} \, \mathrm{d}\Gamma$$

Eliminating $\hat{\boldsymbol{\beta}}$ in the system of equations given by Equation (4), we get

$$\mathbf{K}\hat{\mathbf{u}} = \hat{\mathbf{f}} \tag{5}$$

with

$$\mathbf{K} = \mathbf{G}^t \mathbf{H}^{-1} \mathbf{G}$$

Since the stress interpolation is allowed to be discontinuous across element boundaries, $\mathbf{H}^{-1}$ is composed of distinct block matrices $\mathbf{H}_{(e)}^{-1}$ associated with each element. Thus, the element stiffness matrix is given by

$$\mathbf{K}_{(e)} = \mathbf{G}_{(e)}^t \mathbf{H}_{(e)}^{-1} \mathbf{G}_{(e)} \tag{6}$$

where, with Ω_e denoting the domain of each element,

$$\mathbf{H}_{(e)} = \int_{\Omega_e} \mathbf{P}_{(e)}^t \mathbf{S} \mathbf{P}_{(e)} \, \mathrm{d}\Omega$$

$$\mathbf{G}_{(e)} = \int_{\Omega_e} \mathbf{P}_{(e)}^t \mathbf{B}_{(e)} \, \mathrm{d}\Omega$$

Once the displacement field is found using Equation (5), the stress and strain fields in an element are recovered using the relations

$$\boldsymbol{\tau}_c^{(e)} = \mathbf{P}_{(e)} \hat{\boldsymbol{\beta}}_{(e)} = \mathbf{P}_{(e)} \mathbf{H}_{(e)}^{-1} \mathbf{G}_{(e)} \hat{\mathbf{u}}_{(e)} \tag{7a}$$

$$\boldsymbol{\varepsilon}_c^{(e)} = \mathbf{S}\boldsymbol{\tau}_c^{(e)} = \mathbf{S}\mathbf{P}_{(e)} \mathbf{H}_{(e)}^{-1} \mathbf{G}_{(e)} \hat{\mathbf{u}}_{(e)} \tag{7b}$$

Although we discuss only the static formulation in this work, transient analysis can be carried out by constructing the mass matrix $\mathbf{M}_{(e)} = \int_{\Omega_e} \mathbf{N}_u^t \mathbf{N}_u \, d\Omega$; more accurate results can be obtained by using a dynamic element method as outlined in Reference [15].

The key point in a hybrid formulation is the choice of the stress interpolation matrix $\mathbf{P}_{(e)}$, and we now discuss how it can be chosen in a rational way for the four-node and nine-node elements.

2.1. Four-node element

The shape functions $\mathbf{N}$ in this case are the standard bilinear shape functions expressed in terms of natural co-ordinates (ξ, η). Let the Jacobian matrix be given by

$$\mathbf{J} \equiv \begin{bmatrix} J_{11} & J_{12} \\ J_{21} & J_{22} \end{bmatrix} := \begin{bmatrix} \dfrac{\partial r}{\partial \xi} & \dfrac{\partial z}{\partial \xi} \\ \dfrac{\partial r}{\partial \eta} & \dfrac{\partial z}{\partial \eta} \end{bmatrix} \tag{8}$$

In the case of planar elements, the higher-order terms in $\mathbf{P}$ (which are the linear and quadratic terms in the case of the four-node and nine-node elements, respectively) are chosen so as to prevent zero strain-energy modes in the solution (see, e.g. Reference [16]), and we shall use the same strategy here. The zero-energy modes that result in zero strain at the centre Gauss point $(\xi, \eta) = (0, 0)$ are given by

1. $u_\xi = \alpha_1 \xi\eta, \; u_\eta = 0,$
2. $u_\xi = 0, \; u_\eta = \alpha_2 \xi\eta,$
3. $u_\xi = \alpha_3 \eta, \; u_\eta = -\alpha_3 \xi.$

The first and second zero energy modes can be suppressed by choosing the higher-order terms in $\tau^{\xi\xi}$ and $\tau^{\eta\eta}$ proportional to η and ξ, respectively. Thus, we have

$$\tau^{\xi\xi} = \beta_1 + \beta_4 \eta$$

$$\tau^{\eta\eta} = \beta_2 + \beta_5 \xi$$

$$\tau^{\xi\eta} = \beta_3$$

which is exactly the same interpolation as in the case of a four-node planar element. The third zero-energy mode does not contribute any terms in the case of planar problems (which is the reason that one ends up with a 5β model for planar problems), but it does in the case of axisymmetric problems. Substituting the third zero-energy mode into the transformation relation

$$\begin{bmatrix} u_\xi \\ u_\eta \end{bmatrix} = \mathbf{J} \begin{bmatrix} u_r \\ u_z \end{bmatrix}$$

where $\mathbf{J}$ is given by Equation (8), we get

$$u_r = \frac{\alpha_3}{|\mathbf{J}|}(J_{12}\xi + J_{22}\eta)$$

where $|\mathbf{J}|$ denotes the determinant of $\mathbf{J}$. The contribution of the third-mode to the strain energy is

$$\int_{-1}^{1}\int_{-1}^{1} \frac{u_r}{r}\,\tau_{\theta\theta} r |\mathbf{J}|\,\mathrm{d}\xi\,\mathrm{d}\eta = \int_{-1}^{1}\int_{-1}^{1} \alpha_3 (J_{12}\xi + J_{22}\eta)\tau_{\theta\theta}\,\mathrm{d}\xi\,\mathrm{d}\eta$$

Thus, to suppress the third zero-energy mode, the higher-order term in $\tau_{\theta\theta}$ is chosen to be proportional to $(J_{12}\xi + J_{22}\eta)$, the lower-order term being obviously chosen to be a constant. The final stress-interpolation, after carrying out the appropriate tensor transformations for $(\tau^{\xi\xi}, \tau^{\eta\eta}, \tau^{\xi\eta})$, is now given by

$$\mathbf{P}_{(e)} = \begin{bmatrix} 1 & 0 & 0 & J_{11}^2\eta & J_{21}^2\xi & 0 & 0 \\ 0 & 1 & 0 & J_{12}^2\eta & J_{22}^2\xi & 0 & 0 \\ 0 & 0 & 1 & J_{11}J_{12}\eta & J_{21}J_{22}\xi & 0 & 0 \\ 0 & 0 & 0 & 0 & 0 & 1 & J_{12}\xi + J_{22}\eta \end{bmatrix}$$

We note the following:

1. As is standard practice, the constant parts of $(\tau^{\xi\xi}, \tau^{\eta\eta}, \tau^{\xi\eta})$ are not transformed in order to satisfy patch test requirements. As suggested in References [17, 18], we use the actual Jacobian (and not the Jacobian evaluated at $(\xi, \eta) = (0, 0)$), in order to transform the higher-order terms.
2. Since the formulation is carried out in terms of natural co-ordinates, the resultant element is co-ordinate frame-invariant.
3. Similar to the planar case, basing the design on the zero-energy modes leads very naturally to an element with the minimum number of stress parameters required for stability of the element.
4. The above element is almost identical to the degenerated stress field (DSF) element of Weissman and Taylor [6], although the methodologies used for deriving them are quite different. These authors first derive an eight parameter model, which they call the full stress field (FSF) element, and then drop one term based on numerical experiments to come up with the DSF model. The DSF element has an additional term of the form $(\partial z/\partial h)h$, where $h := \xi\eta$, in the field corresponding to β_7. However, this term does not seem to contribute much, and the difference in results obtained using the DSF and our element are marginal.

2.2. Nine-node element

The spurious zero-energy modes at the Gauss points $(\xi, \eta) = (\pm 1/\sqrt{3}, \pm 1/\sqrt{3})$ are

1. $u_\xi = \alpha_1(1 - 3\xi^2)(1 - 3\eta^2),\ u_\eta = 0,$
2. $u_\xi = 0,\ u_\eta = \alpha_2(1 - 3\xi^2)(1 - 3\eta^2),$
3. $u_\xi = \alpha_3\xi(1 - 3\eta^2),\ u_\eta = -\alpha_3\eta(1 - 3\xi^2).$

The first two zero-energy modes lead to the stress field

$$\tau^{\xi\xi} = \beta_1 + \beta_4\xi + \beta_7\eta + \beta_{10}\xi\eta + \beta_{13}\xi\eta^2$$

$$\tau^{\eta\eta} = \beta_2 + \beta_5\xi + \beta_8\eta + \beta_{11}\xi\eta + \beta_{14}\xi^2\eta$$

$$\tau^{\xi\eta} = \beta_3 + \beta_6\xi + \beta_9\eta + \beta_{12}\xi\eta$$

which is exactly the same as in the case of a planar hybrid nine-node element. The third zero-energy mode is non-communicable [16], and hence can be discarded (the implication is that this mode is suppressed when there are two or more elements in a mesh, or when boundary conditions prevent this mode in a single element mesh). Since there are no additional zero-energy modes, the natural choice for interpolating $\tau_{\theta\theta}$ (which also suppresses the lower-order modes that occur in the four-node element) is the set $(1, \xi, \eta)$. Thus, we have

$$\mathbf{P}_{(e)} = \begin{bmatrix} \mathbf{I}_{3\times3} & \xi\mathscr{F}_1 & \xi\mathscr{F}_2 & \xi\mathscr{F}_3 & \eta\mathscr{F}_1 & \eta\mathscr{F}_2 & \eta\mathscr{F}_3 & \xi\eta\mathscr{F}_1 & \xi\eta\mathscr{F}_2 & \xi\eta\mathscr{F}_3 & \xi\eta^2\mathscr{F}_1 & \xi^2\eta\mathscr{F}_2 & 0 & 0 & 0 \\ \mathbf{0}_{1\times3} & 0 & 0 & 0 & 0 & 0 & 0 & 0 & 0 & 0 & 0 & 0 & 1 & \xi & \eta \end{bmatrix}$$

where

$$\mathscr{F}_1 = \begin{Bmatrix} J_{11}^2 \\ J_{12}^2 \\ J_{11}J_{12} \end{Bmatrix}, \quad \mathscr{F}_2 = \begin{Bmatrix} J_{21}^2 \\ J_{22}^2 \\ J_{21}J_{22} \end{Bmatrix}, \quad \mathscr{F}_3 = \begin{Bmatrix} 2J_{11}J_{21} \\ 2J_{12}J_{22} \\ J_{11}J_{22} + J_{12}J_{21} \end{Bmatrix}$$

Note again that the actual Jacobian is used in the above expressions.

3. NUMERICAL EXAMPLES

In this section, we present several examples (some of which have been proposed by MacNeal and Harder [19]) to show the good performance of the four-node and nine-node elements, referred to subsequently as A4 and A9. As already pointed out, the results obtained using the A4 element are almost identical to the ones obtained using the DSF element of Reference [6], and hence we shall present results only for the elements that have been developed in this work. To ensure a fair comparison of results between the A4 and A9 elements, we use meshes with identical number of nodes on any given problem, i.e. four times as many A4 elements as A9 elements are used in the comparison of the results. The stresses are computed *directly* using Equation (7a), and not from an extrapolation using the Gauss point values as is usually done. Standard Gaussian quadrature, i.e. a 2×2 rule for the A4 and a 3×3 rule for the A9 element, is used for constructing the stiffness matrices, and, in addition, consistent load vectors and uniform meshes are used in all examples. The mesh densities are written as $m \times n$ with m denoting the number of elements in the radial direction.

3.1. Patch test

Both elements A4 and A9 have been developed in a manner such that they will pass the patch test. As a numerical confirmation, we use the mesh in Reference [10], and a similar mesh for the A9 element. Both elements pass the patch test. In addition, both elements are insensitive to the order of nodal point numbering.

3.2. Thick-walled cylinder

A thick-walled cylinder of unit thickness, and inner radius 3 and outer radius 9 is subjected to a unit internal pressure under plane strain conditions [19] (see Figure 1). The Young modulus is 1000, and the Poisson ratio is 0.499 (almost incompressible material). The analytical solutions for the radial displacement and the non-zero stress components ($\tau_{rr}, \tau_{zz}, \tau_{\theta\theta}$) at the inner surface are 5.060249×10^{-3} and $(-1, 0.12475, 1.25)$, respectively. Similar to the DSF element, we get the exact nodal displacements and τ_{zz} solution, even with a single element when we use a regular mesh; hence, we present the normalized results only for the τ_{rr} and $\tau_{\theta\theta}$ components. Since the field variables vary only along the radial direction in this example, we use meshes with three nodes along the thickness, and $3, 5$ and 9 nodes along the radial direction; the results are presented in Table I.

Quite unfortunately, a direct comparison of our results with those obtained using other formulations is not always possible because of the different geometries, material properties and mesh discretizations used. However, to the best of our knowledge, the DSF element [6] is the only other type of element that yields superconvergent results for the displacements. Spilker [3], Sze *et al*. [9], Wanji *et al*. [10] and Kasper *et al*. [11] (who use a mixed-enhanced formulation) report errors of 0.13, 0.5, 1.4 and 4.5%, respectively, for the displacement at the inner surface.

The normalized results for the displacements at point A for the distorted mesh shown in Figure 1 are 0.996975 and 1.00276 for the A4 and A9 elements, respectively. Thus, one sees that both elements are quite immune to mesh distortion.

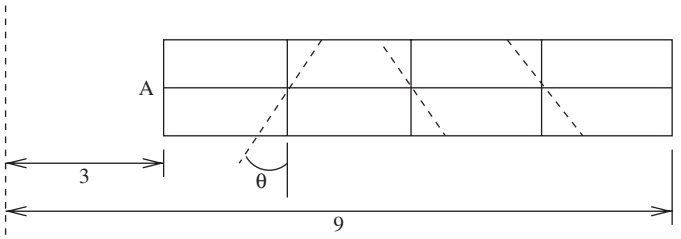

Figure 1. Thick-walled cylinder subjected to uniform internal pressure under plane strain conditions. The domain is shown modelled using a 4×2 A4 mesh; the distorted mesh used with $\theta = 26.565°$ is shown by dotted lines.

Table I. Normalized stresses at the inner radius in the thick-cylinder problem.

	τ_{rr}		$\tau_{\theta\theta}$	
Nodes/radial dirn.	A4	A9	A4	A9
3	0.4375	0.6250	0.55	0.70
5	0.6250	0.8125	0.70	0.85
9	0.7750	0.9250	0.82	0.94

3.3. Thick sphere subjected to internal pressure

A thick sphere of inner radius 1 and outer radius 5 is subjected to a unit internal pressure. The material properties are $E = 1000$ and $v = 0.499$. Uniform meshes of 4×4 and 8×8 A4, and 2×2 and 4×4 A9 meshes are used (see Figure 2). The analytical solution for the radial displacement is 7.5556×10^{-4}. The normalized results obtained are presented in Table II. Note the high accuracy of the A9 element even with a coarse mesh, and its rapid convergence to the analytical solution with mesh refinement. Note also the reasonably good symmetry in the displacement values at points A and B with both types of elements.

Kasper and Taylor [11] use a sphere with inner and outer radii given by 1 and 2, respectively, and $E = 250$. For $v = 0.49999$, and with meshes of 1×2 and 2×4, they obtain normalized displacements at the top point on the inner surface as 0.84 and 0.94, respectively, while, with the same discretizations, we obtain normalized solutions of 0.90 and 0.99 using the A4 element.

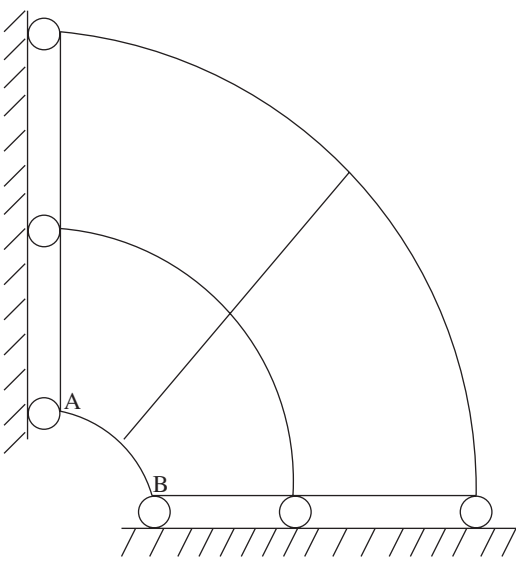

Figure 2. Thick sphere subjected to internal pressure; a quarter of the domain is shown modelled using a uniform 2×2 A9 mesh.

Table II. Normalized radial displacement at the inner surface in the thick-sphere problem.

	Point A		Point B	
Nodes/side	A4	A9	A4	A9
5	0.79421	1.11924	0.81294	0.98095
9	0.92540	1.01658	0.92718	0.99552

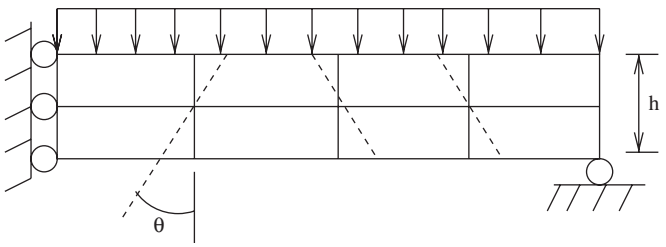

Figure 3. Simply-supported circular plate subjected to uniform pressure. The domain is shown modelled using a 4×2 A4 mesh; the distorted mesh used with $\theta = 26.565°$ is shown by dotted lines.

Table III. Normalized centre-point displacements in the circular plate problem; values in parenthesis are the results obtained with the distorted mesh.

	$h = 1$		$h = 0.01$	
Nodes/radial dirn.	A4	A9	A4	A9
5	1.02418	1.03762	1.02531	1.03860
	(0.95197)	(1.02780)	(0.22951)	(1.03373)
9	1.00749	1.00670	1.00845	1.00798

3.4. Thick and thin simply-supported plates

The purpose of this example is to show that both elements are immune to shear locking as the thickness is reduced. A simply-supported circular plate of radius 10 and with $\nu = 0.3$ is subjected to a unit pressure load on the top surface as shown in Figure 3. Two cases are considered (i) $E = 10^4$, $h = 1$ ('thick plate'), and (ii) $E = 10^{10}$, $h = 0.01$ ('thin plate'). The analytical solutions for the centre-point deflection are 0.70388 and 0.69563, respectively. Uniform meshes of 4×2 and 8×2 A4 elements, and 2×1 and 4×1 A9 elements are used. The distorted mesh used in Reference [6] is shown by dotted lines in Figure 3. The normalized results for the centre-point deflection are presented in Table III. As can be seen, with a regular mesh, both elements are almost immune to mesh distortion, and to shear-locking even when the thickness/radius ratio is as small as 1/1000. When a distorted mesh is used, the A4 element displays signs of locking on the thin plate (similar to the DSF element), while the A9 yields a good result even in this case.

For comparison purposes, we have tried the various Poisson ratios and mesh distortions used in Reference [10] (their Figure 3 and Tables V–VII), and found that our results are almost identical to theirs.

To obtain an idea of the spatial distribution of the displacement field, the transverse displacements at the nodal points along the axis of the thick plate are listed in Table IV.

3.5. Spinning disc

A solid disc of radius 4 and unit thickness, whose top and bottom surfaces are constrained so as to allow only radial motion, is spun about its axis with a constant angular velocity ω such that

Table IV. Transverse displacements at the nodal points along the axis of the mesh shown in Figure 3 with $h = 1$.

Element type	1	2	3	4	5
A4	−0.7209	−0.6479	−0.4886	−0.2599	−0.0008
A9	−0.7304	−0.6682	−0.5108	−0.2729	−0.0049

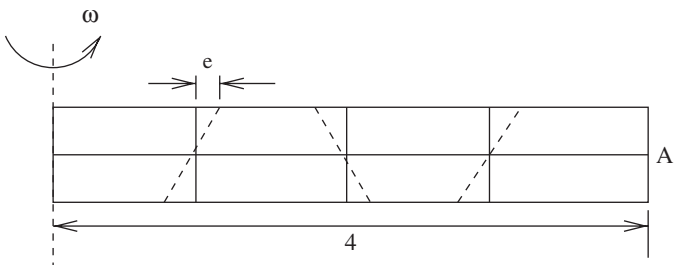

Figure 4. Disc spinning with uniform angular speed. The domain is shown modelled using a 4×2 A4 mesh; the distorted mesh used with $e = 0.05$ is shown by dotted lines.

Table V. Normalized stresses at the axis in the spinning disc problem.

	τ_{rr}		τ_{zz}	
Nodes/radial dirn.	A4	A9	A4	A9
5	0.99913	1.07354	0.99913	1.07354
9	1.00341	1.01829	1.00341	1.01829

$\rho\omega^2 = 100$ (see Figure 4). The material properties are $E = 1000$ and $\nu = 0.499$. The analytical solution for the radial displacement at the outer edge is 4.79674×10^{-3}, while the stresses $(\tau_{rr}, \tau_{zz}, \tau_{\theta\theta})$ at the axis are given by (799.2016, 797.6032, 799.2016). Uniform meshes of 4×2 and 8×2 A4 elements, and 2×1 and 4×1 A9 elements are used. With the uniform mesh, both elements yield the exact displacements at the periphery (but in contrast to the thick-cylinder problem, the displacement solution is not exact at the intermediate nodes), even with the use of only one element. With the distorted mesh, we get the normalized displacements at point A with the A4 and A9 elements as 1.05463 and 1.091, respectively. With the regular mesh, the $\tau_{\theta\theta}$ component in the finite element solution is equal to the τ_{rr} component in accordance with the exact solution, and hence only the normalized results for the τ_{rr} and τ_{zz} component are presented in Table V. While it may appear that the four-node element yields more accurate stresses than the nine-node one, it is only at certain points that this is true. For example, at

the outer free surface of the disc where $\tau_{rr} = 0$, the A9 element yields a much more accurate value of 27.75 compared with the value of 168.60 given by the A4 element.

4. CONCLUSIONS

A general methodology for the development of hybrid axisymmetric elements based on zero-energy modes is proposed. We show that with this methodology, it is possible to develop elements with the minimum number of stress parameters that are required to obtain the correct rank of the stiffness matrix, thus keeping the cost of element stiffness matrix formation to a minimum. A point that we would like to emphasize is that the stress interpolation functions obtained by this procedure involve only a small change over and above the stress interpolation functions for a planar element, thus making them easy to implement within the same framework; in fact for the four-node and nine-node axisymmetric elements that we have designed using this procedure, it turns out that the interpolations for the in-plane stress components are identical to those for the corresponding planar elements. Both these elements perform well, even under pathological situations.

REFERENCES

1. Feng W, Hoa SV, Huang Q. Classification of stress modes in assumed stress fields of hybrid finite elements. *International Journal for Numerical Methods in Engineering* 1997; **40**:4313–4339.
2. Spilker RL, Pian THH. A study of axisymmetric solid of revolution elements based in the assumed-stress hybrid model. *Computers and Structures* 1978; **9**:273–279.
3. Spilker RL. Improved hybrid-stress axisymmetric elements including behavior for nearly incompressible materials. *International Journal for Numerical Methods in Engineering* 1981; **17**:483–501.
4. Renganathan K, Rao BN, Jana MK. An efficient axisymmetric hybrid-stress-displacement formulation for compressible/nearly incompressible material. *International Journal of Pressure Vessels and Piping* 2000; **77**:651–667.
5. Bachrach WE, Belytschko T. Axisymmetric elements with high coarse-mesh accuracy. *Computers and Structures* 1986; **23**:323–331.
6. Weissman SL, Taylor RL. Four-node axisymmetric element based upon the Hellinger–Reissner functional. *Computer Methods in Applied Mechanics and Engineering* 1991; **85**:39–55.
7. Tian Z, Pian THH. Axisymmetric solid elements by a rational hybrid stress method. *Computers and Structures* 1985; **20**:141–149.
8. Wanji C, Cheung YK. Axisymmetric solid elements by the generalized hybrid method. *Computers and Structures* 1987; **27**(6):745–752.
9. Sze KY, Chow CL. An incompatible element for axisymmetric structure and its modification by hybrid method. *International Journal for Numerical Methods in Engineering* 1991; **31**:385–405.
10. Wanji C, Cheung YK. The noncomforming element method and refined hybrid element method for axisymmetric solid. *International Journal for Numerical Methods in Engineering* 1996; **39**:2509–2529.
11. Kasper EP, Taylor RL. Mixed-enhanced formulation for geometrically linear axisymmetric problems. *International Journal for Numerical Methods in Engineering* 2002; **53**:2061–2086.
12. Hughes TJR. *The Finite Element Method*: *Linear*, *Static and Dynamic Finite Element Analysis*. Dover Publications: New York, 2000.
13. Johnson C. *Numerical Solution of Partial Differential Equations by the Finite Element Method*. Cambridge University Press: Cambridge, MA, 1987.
14. Simo JC, Kennedy JG, Taylor RL. Complementary mixed finite element formulations for elastoplasticity. *Computer Methods in Applied Mechanics and Engineering* 1989; **74**(2):177–206.
15. He G, Chen D, Pian THH. Incompatible finite dynamic element formulation for free vibration analysis by hybrid stress formulation. *Communications in Numerical Methods in Engineering* 2000; **16**:293–299.

16. Lee SW, Rhiu JJ. A new efficient approach to the formulation of mixed finite element models for structural analysis. *International Journal for Numerical Methods in Engineering* 1986; **23**:1629–1641.
17. Jog CS. Higher-order shell elements based on a Cosserat model, and their use in the topology design of structures. *Computer Methods in Applied Mechanics and Engineering* 2004; **193**:2191–2220.
18. Punch EF, Atluri SN. Development and testing of stable, invariant, isoparametric curvilinear 2- and 3-d hybrid-stress elements. *Computer Methods in Applied Mechanics and Engineering* 1984; **47**:331–356.
19. MacNeal RH, Harder RL. A proposed standard set of problems to test finite element accuracy. *Finite Elements in Analysis and Design* 1985; **1**:3–20.

